Bridging-Coupling Phenomenon in Linear Elastic Metamaterials by Exploiting Locally Resonant Metachain Isomers

Danilo Beli[1,*] Massimo Ruzzene[2] and Carlos De Marqui, Jr.[1]

[1]*São Carlos School of Engineering, University of São Paulo, São Carlos-SP 13563-120, Brazil*
[2]*Department of Mechanical Engineering, University of Colorado Boulder, Colorado 80309, USA*

Elastic and acoustic metamaterials are man-made structures designed to control and manipulate waves through band gaps. The generalized bandwidth of metamaterials with locally resonant (LR) band gaps is usually narrow, limiting their applications in noise and vibration control. On the other hand, nonlinear metamaterials with dipolar resonances can present a broad chaotic band with low amplitude resonances due to bridging coupling, which is only observed under sufficiently large excitation amplitudes. In this work, we show that bridging-coupling phenomenon can also be observed in linear metamaterials with dipolar resonance, producing a special pass band with low amplitude resonances at low frequencies without excitation amplitude dependence. Such phenomenon emerges in a modified resonant metachain with zigzag interconnections and is based on the isomerism of traditional metamaterials. Although this modified isomer preserves the static stiffness and mass density (i.e., static performance) of the original metamaterial, its dispersive behavior presents interesting properties (i.e., branches with negative mass features and overlapping of opposite group velocity), resulting in an overall negative effective mass between the LR band gaps that is responsible for the remote interaction and the enhanced wave performance. In addition to the theoretical discussions, the bridging coupling is experimentally observed in a three-dimensional printed elastic metamaterial rod supporting longitudinal waves. The design can be extended to elastic bending, acoustic and electromechanical media, as well as to systems with periodicity in two and three dimensions (i.e., plates and solids). Therefore, the findings of this work open avenues to investigate the bridging-coupling phenomenon in linear systems as well as to explore the properties of metamaterial isomers.

I. INTRODUCTION

Phononic crystals and metamaterials have been used to attenuate and manipulate acoustic and elastic waves through band gaps, frequency bands where the waves cannot propagate [1–3]. These periodic structures present a vast range of applications that include vibration and noise isolation, acoustic cloaking, phase manipulation, wave guiding, and focalization [4–7]. In phononic crystals, the band gap is produced by Bragg scattering, which is related to spatial periodicity of material or geometrical properties that scatter waves with wavelength at the same order of the unit-cell length [8,9]. In locally resonant (LR) metamaterials, the band gap is created by Mie-type and Fabry-Perot-type resonances due to arrays of local resonators tuned to frequencies without dependence to the unit-cell length [10,11]. These internal resonances provide unique properties to the lattice (e.g., negative refraction [12], negative effective mass, and negative effective bulk

modulus [13–17]) that cannot be found in conventional materials. However, the generalized bandwidth of LR band gaps (i.e., ratio of the bandwidth to its start frequency) is narrow and depends on the ratio of added mass of the attached resonators to the original mass of the host structure, limiting its applications in noise and vibration control, where a broadband attenuation at low frequencies is desired [18–20].

Several approaches have been proposed to improve the attenuation bandwidth performance of LR metamaterials. Some of them explore adjacent band gaps by placing a LR band gap closer to a Bragg band gap or closer to another LR band gap. This concept has been applied to metamaterials with multiple resonances [21], resonators interaction to achieve multiband gaps [22,23], metadamping [24], or with random or correlated disorder in rainbow configurations [25,26]. Although these adjacent band gaps improve the overall vibration attenuation bandwidth, the width of each single band gap is still narrow [3,5]. Moreover, vibration modes can emerge at the pass bands between the band gaps or can be localized at band gap boundaries as

---

*beli.danilo@gmail.com

a consequence of the typical flat branches of LR metamaterials. As an alternative, the translational and rotational coupled motion of single resonators, as in chiral and inertial metamaterials, produce a double negative band gap and also a broadband vibration attenuation [18,27]. The hybridization phenomena, which emerge in coupled waves or in a metachain made of local resonances interacting with the host structure wave, also provide a broadband vibration attenuation [28–30]. Recently, the hybridization phenomena using resonant networks with coupled translational (mass) and rotational (inertia) motions have also been explored to open large band gaps in beams and plates, [31] and the concept has been employed in lattice systems [32,33].

Furthermore, metamaterials possessing nonlinear local resonators have also been used to achieve unusual and unconventional wave attenuation and manipulation by exploring different physical phenomena, which includes solitons, amplitude-dependent band gaps, harmonic energy transfer, and nonreciprocal behavior [34–40]. One of these unusual phenomena is the bridging coupling, a special pass band zone with low amplitude resonances observed between the linearized LR band gaps. This effect emerges due to chaotic bands that work like the floor (or deck) of a bridge promoting the remote interactions between the LR band gaps, which are the foundations (or pillars) of the bridge. Although nonlinear phenomenon possesses a double ultra chaotic band (i.e., a ultra broadband with low amplitude resonances at ultralow frequencies), and, hence, a superior wave and vibration performance [19,41], the bridging coupling is only activated under sufficiently large excitation amplitudes.

In this work, the bridging-coupling phenomenon, which is also defined as the bridging-coupling frequency range due to the special pass band with low amplitude resonances, is explored and observed in linear acoustic and elastic metamaterials. A metamaterial with zigzag interconnected resonant metachain based on the isomerism of the traditional metamaterial with dipolar resonance is proposed. Although this isomer preserves the static stiffness and mass density of the original metamaterial, its dispersive behavior has unique properties. Dispersive branches with negative effective mass and noteworthy features emerge due to an unusual interaction between the resonators, promoting a remote interaction between the linear local resonances and, therefore, creating a special broad pass band with low amplitude resonances. This linear bridging-coupling phenomenon differs from the adjacent band gap and from traditional hybridization phenomena (i.e., locking or veering), and it is similar to the nonlinear metamaterial case where the nonlinear bridging coupling is only observed for certain excitation levels. Herein, the remote interaction between LR band gaps in resonant metachains is explored and, therefore, the unusual dispersive branches work like the chaotic band. A metamaterial

supporting only longitudinal motion is investigated, and, hence, our findings can also be extended to bending waves as well as to acoustic and electromechanical media. This demonstration can open alternative avenues to investigate the bridging-coupling phenomenon in linear systems as well as the dynamical properties of metamaterial isomers.

II. LOCALLY RESONANT METACHAIN ISOMERS AND THE BRIDGING-COUPLING PRINCIPLE

A. Governing equations

Considering the masses as atoms and the springs as interatomic links [42], all periodic configurations in Fig. 1 present the same molecular formula and the same spatial atomic set, but different structural architecture that are repeated periodically, i.e., they are periodic structural isomers. Hence, the lattice topology completely changes, providing a particular wave propagation and dynamic behavior for each metachain isomer, although, their static stiffness and mass density are preserved (i.e., static performance). The one-dimensional lattice configuration composed of three masses in Fig. 1(a) corresponds to the traditional metamaterial and it is the initial isomer, where one mass corresponds to the host lattice ($m_p^h - k_p^h$) and the other two represent two local resonators in series ($m_p^a - k_p^a$ and $m_p^b - k_p^b$). When these resonator masses are interconnected to adjacent unit-cell resonators by a spring k^c, as shown in Figs. 1(b) and 1(c), making a metachain, the zero group velocity of the flat branches with negative effective mass features related to the local resonances become nonzero, and, hence, the waves propagate in the resonant network and interact nonlocally with the wave propagating in the host lattice [28,31]. Moreover, in the straight interconnection of Fig. 1(b), the resonant masses interact with the correspondent resonant masses of the adjacent
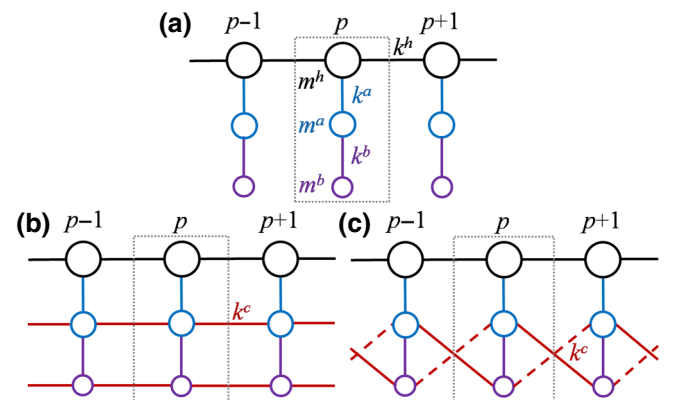

FIG. 1.   One-dimensional isomer models: (a) dipolar resonator, (b) resonant metachain with straight interconnections, and (c) resonant metachain with zigzag interconnections, where all the point masses are constrained to move horizontally and all interatomic links represent longitudinal springs.

unit cells (i.e., $m_p^a \leftrightarrow m_{p-1,p+1}^a$ and $m_p^b \leftrightarrow m_{p-1,p+1}^b$), while in the zigzag interconnection of Fig. 1(c), the resonant masses interact with different resonant masses of the adjacent unit cells (i.e., $m_p^a \leftrightarrow m_{p-1,p+1}^b$ and $m^b \leftrightarrow m_{p-1,p+1}^a$). This triatomic model can be analysed within a general framework in order to investigate the dynamic behavior of interest, which includes the dispersion analysis, effective properties and forced response, and their relation with the bridging coupling in linear metamaterials. The governing equations of motion of the metamaterial systems composed of the host lattice and a resonant network (i.e., metachain), regardless of the architecture, can be written as

$$m^h \ddot{u}_p^h + (2k^h + k^a)u_p^h - k^a u_p^a - k^h(u_{p-1}^h + u_{p+1}^h) = f_p^h, \quad (1a)$$

$$m^a \ddot{u}_p^a + (k^a + k^b + 2k^c)u_p^a - k^a u_p^h - k^b u_p^b + \cdots$$
$$- k^c(u_{p-1}^{\alpha_1} + u_{p+1}^{\alpha_1}) = f_p^a, \quad (1b)$$

$$m^b \ddot{u}_p^b + (k^b + 2k^c)u_p^b - k^b u_p^a - k^c(u_{p-1}^{\alpha_2} + u_{p+1}^{\alpha_2}) = f_p^b. \quad (1c)$$

For dipolar resonance, the resonator masses are disconnected from those in the neighborhoods; therefore, $k^c = 0$. When the resonator masses are connected to the adjacent masses, making a metachain, $k^c \neq 0$. Moreover, the network can present straight ($\alpha_1 = a$ and $\alpha_2 = b$) or zigzag ($\alpha_1 = b$ and $\alpha_2 = a$) interconnections between the resonant masses m^a and m^b. Several architectures may be obtained from the original architecture with independent resonators in Fig. 1(a). The dynamics of all of them, however, can be understood from the three basic isomers presented in this section.

B. Dispersion analysis

The plane waves propagating in the lattices are investigated by imposing the Bloch-Floquet periodic solution in the form $\mathbf{u}_p(t) = \mathbf{u}_0 e^{i(\omega t - \kappa a p)}$ (where ω is the angular frequency, κ is the wave number, a is the unit-cell lattice length, $\mathbf{u}_p = [u_p^h, u_p^a, u_p^b]$ is the displacement vector, and i is the imaginary number) on the homogeneous equations of motion (i.e., $f_p^h = f_p^a = f_p^b = 0$), which leads to the following eigenvalue problem in the form $\omega(\kappa)$: $\mathbf{K}(\kappa)\mathbf{u}(\kappa) = \omega^2 \mathbf{M}\mathbf{u}(\kappa)$ with

$$\mathbf{K}(\kappa) = \begin{bmatrix} 2k^h - \beta^h + k^a & -k^a & 0 \\ -k^a & k^a + k^b + 2k^c - \beta^l & -k^b - \beta^c \\ 0 & -k^b - \beta^c & k^b + 2k^c - \beta^l \end{bmatrix} \quad \text{and} \quad \mathbf{M} = \begin{bmatrix} m^h & 0 & 0 \\ 0 & m^a & 0 \\ 0 & 0 & m^b \end{bmatrix}. \quad (2)$$

Here $a = 1$ for convenience and $\beta^h = 2\zeta k^h$ with $\zeta = \cos(\kappa a)$. Moreover, for independent resonators, $k^c = 0$, $\beta^l = 0$, and $\beta^c = 0$, for a straight interconnection, $\beta^l = 2\zeta k^c$ and $\beta^c = 0$, and for a zigzag interconnection, $\beta^l = 0$ and $\beta^c = 2\zeta k^c$. In the dispersion analysis, the angular frequencies $\omega(k)$ and the wave mode shapes $\mathbf{u}(\kappa)$ are obtained by varying the wave number within the irreducible Brillouin zone (IBZ), i.e., $\mathrm{Re}[\kappa] = [0, \pi/a]$, which carries the wave information of the periodic lattice.

Besides the band structure computation, the effective mass calculation also becomes necessary to understand the physical mechanism of the wave attenuation on the proposed metamaterial lattice, since a strong wave attenuation appears when the effective mass diverges to a high value or becomes negative [5]. Because of the multilayer configuration and interconnections, the effective mass is nonlocal [43] (i.e., it also has a spatial dependency); hence, this effective parameter is not only dependent on the frequency, but also dependent on the wave number [44,45]: $\overline{m}_{\mathrm{eff}}(\omega, \kappa)$. By using the matrices in Eq. (2), a secular equation that describes the effective properties as a function of angular frequency and wave number can also be found [16]. By solving the system of equations

and considering $f_0^h = (2k^h - \beta^h)u_0^h$ [15], the dispersive effective mass is given by

$$\overline{m}_{\mathrm{eff}}(\omega, \kappa) = -\frac{1}{\omega^2}\frac{\langle f_0^h \rangle}{\langle u_0^h \rangle} = m^h - \frac{k^a}{\omega^2}\left(1 - \frac{\omega_a^2}{\overline{\omega}_k^2}\right), \quad (3)$$

where $\overline{\omega}_k^2$ is given by

$$\overline{\omega}_{\mathrm{I}}^2 = \omega_a^2 + \omega_{ba}^2 - \omega^2 - \frac{\omega_b^2 \omega_{ba}^2}{\omega_b^2 - \omega^2},$$

$$\overline{\omega}_{\mathrm{S}}^2 = \omega_a^2 + \omega_{ba}^2 + 2\omega_{ca}^2(1 - \zeta) - \omega^2$$
$$- \frac{\omega_b^2 \omega_{ba}^2}{\omega_b^2 + 2\omega_{cb}^2(1 - \zeta) - \omega^2},$$

$$\overline{\omega}_{\mathrm{Z}}^2 = \omega_a^2 + \omega_{ba}^2 + 2\omega_{ca}^2 - \omega^2$$
$$- \frac{\omega_b^2 \omega_{ba}^2 + 2\omega_b^2 \omega_{ca}^2 \zeta + \omega_{ca}^2 \omega_{cb}^2 \zeta^2}{\omega_b^2 + 2\omega_{cb}^2 - \omega^2},$$

for the isomer with independent resonators, straight interconnection, and zigzag interconnection, respectively;

moreover, $\omega_a = \sqrt{k^a/m^a}$, $\omega_b = \sqrt{k^b/m^b}$, $\omega_{ba} = \sqrt{k^b/m^a}$, $\omega_{ca} = \sqrt{k^c/m^a}$, $\omega_{cb} = \sqrt{k^c/m^b}$. Therefore, the effective mass for each branch can be obtained by replacing the (ω, κ) pair in Eq. (3), which is evaluated within the IBZ for the desirable angular frequency window. By using both the $\overline{m}_{\rm eff}(\omega, \kappa)$ map and the band structure, it is possible to determine if a wave branch presents positive or negative effective mass feature, and, hence, relate it to the wave attenuation.

For numerical purposes, the parameters in Eq. (1) are $m^h = 1$, $m^a = 0.2$, $m^b = 0.1$, $k^h = 20000$, $k^a = 50$, $k^b = 10$, and $k^c = 12.5$. Moreover, the wave number and the angular frequency are respectively normalized as $\mu = \kappa a/\pi$ and $\Omega = \omega a/c_h$, where $c_h = \sqrt{k^h/m^h}$ is the speed of the wave propagating in the host lattice. The wave behavior and the effective mass features in κ-ω space for the three isomers are depicted in Fig. 2. As expected [46], the independent case shown in Fig. 2(a) presents two flat branches due to the dipolar characteristic of the local resonator; when these nondispersive waves with zero group velocity interact with the host lattice wave, two LR band gaps with negative effective mass emerge. This effective wave presents a high imaginary component responsible for the vibration attenuation at the LR band gap frequencies. Regarding the wave mode shapes shown in Fig. 2, although the resonant masses affect both negative branches, the first LR band gap is dominated by the resonant mass m^b and an in-phase mode ($I.1$ to $I.3$), while the second LR band gap is dominated by the resonant mass m^a and an out-of-phase mode ($I.4$ to $I.6$).

When the dipolar resonators are interconnected to each other, changing the architecture of the original isomer, waves also propagate in the resonant network and interact with the wave propagating in the host lattice, which can lead to hybridization band gaps [28,47] through veering and locking effects [48] as well as to other unexplored wave phenomena, such as this demonstration of bridging coupling in linear metamaterials.

For the straight interconnection, the resonant network waves propagate and hybridize with the host wave, as shown in Fig. 2(b). This resonant network presents only branches with positive group velocity that weakly interact between them, and also weakly interact with the host lattice wave, in both cases through the veering effect. Despite the fact that the in-phase and out-of-phase wave mode shapes are still related to each resonant branch [as in the independent case of Fig. 2(a)], the resonator mass amplitude related to vibration absorption (of the host mass) in each branch is inverted from low to high frequencies (as observed from $S.1$ to $S.3$ and from $S.4$ to $S.6$), due to veering phenomenon between the resonant branches. However, the network waves are strongly affected by negative effective mass features closer to the host lattice wave due to the dominance of the local resonances.
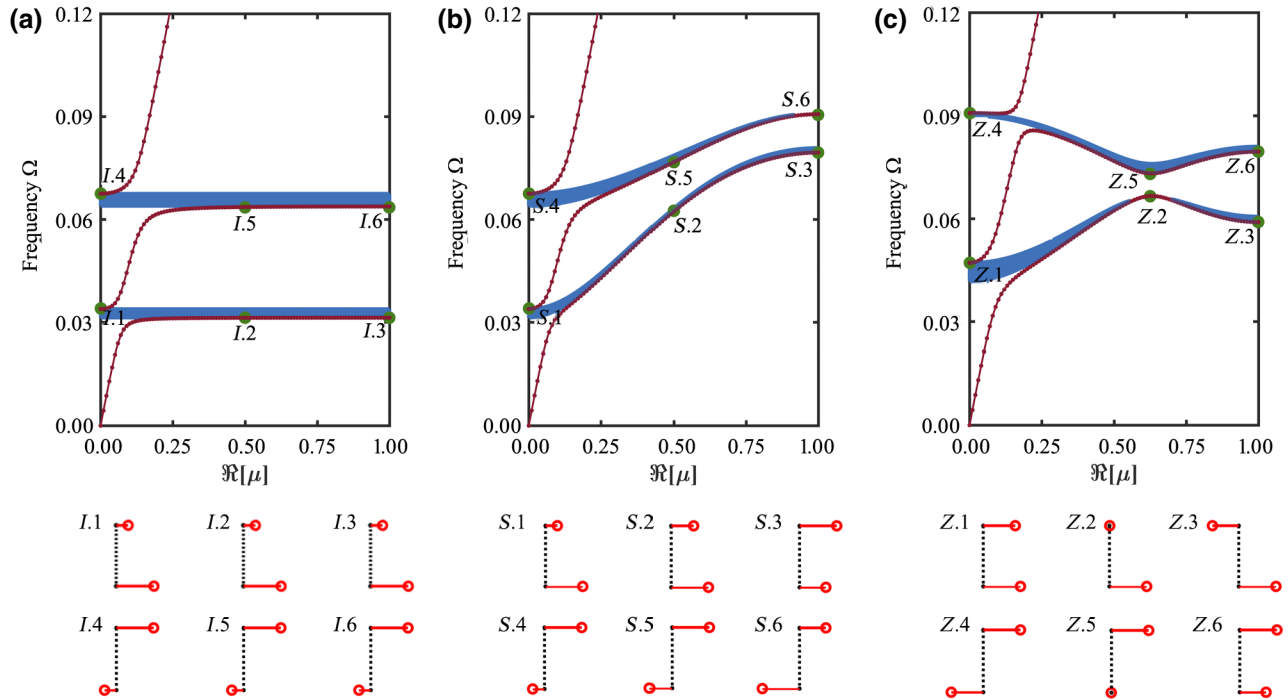

FIG. 2. Band structure and wave mode shapes for (a) independent resonators I, (b) straight interconnection S, and (c) zigzag interconnection Z. Red circles represent propagating waves and blue shaded areas represent the negative effective mass zones in κ-ω space obtained from Eq. (3).

The isomer with zigzag interconnection presents one resonant branch with positive group velocity and another with negative group velocity [see Fig. 2(c)], indicating that the wave modes of the metachain carry energy in opposite directions [48]. The metachain branches interact with each other, which leads to a small coupling band gap opening at $\Omega \approx 0.07$, along with hybridization band gaps: one due to veering at $\Omega \approx 0.04$, and one due to locking at $\Omega \approx 0.09$. Moreover, the resonant branches with negative effective mass features and opposite group velocity (i.e., abnormal behavior [49]) connect the two LR band gaps in the κ-ω space. Regarding the mode shapes, we note that (i) both resonant masses present high vibration amplitude at low and high frequencies in both wave modes, and (ii) while the in-phase mode preserves the positive group velocity ($Z.1$, $Z.2$, and $Z.6$), the out-of-phase mode exhibits negative group velocity ($Z.4$, $Z.5$, and $Z.3$). When these metachain branches interact with the host branch, the veering presents a negative effective mass feature, while the locking has a positive effective mass feature. Moreover, a branch with negative effective mass due to the resonant network crosses through the locking zone at $\Omega \approx 0.09$.

C. Forced response of the finite chain

The dynamic behavior related to each isomer is performed using the harmonic (steady state) response of a finite lattice composed of 100 unit cells for numerical purposes. A unitary harmonic displacement excitation is imposed at one end (i.e., unit cell $p = 1$) and the measured displacement is obtained at the other end (i.e., unit cell $p = 100$), with both the excitation and measurement placed in the host masses. First, consider the lattices without damping in the interconnections; the transmission responses τ in decibels, i.e., $20 \log_{10}|u_{\text{out}}/u_{\text{in}}|$, are presented in Figs. 3(a) and 3(d). The three architectures exhibit the same vibration behavior at low frequencies, which means that the static stiffness and the mass density are preserved between the periodic isomers. Moreover, high density resonant zones composed of resonances and antiresonances that are associated to the nonlocal negative effective mass branches (and not related to the hybridization band gaps, i.e., veering and locking) appear in the forced response. From the interaction of the host branch (positive effective mass) with the resonant branches (negative effective mass), which present wave attenuation features, emerges a frequency zone where the energy is continually exchanged between the host lattice and the resonant network. This analysis could lead to the incorrect conclusion that interconnected configurations deteriorate the dynamic behavior of the host lattice. One important remark is that even with resonant zones created in both isomers with interconnections between the resonators, the wave interaction is stronger in the isomer with zigzag interconnections [$0.04 < \Omega < 0.09$ in Fig. 3(d)] than in the isomer with straight interconnections [$0.03 < \Omega < 0.08$ in Fig. 3(a)].
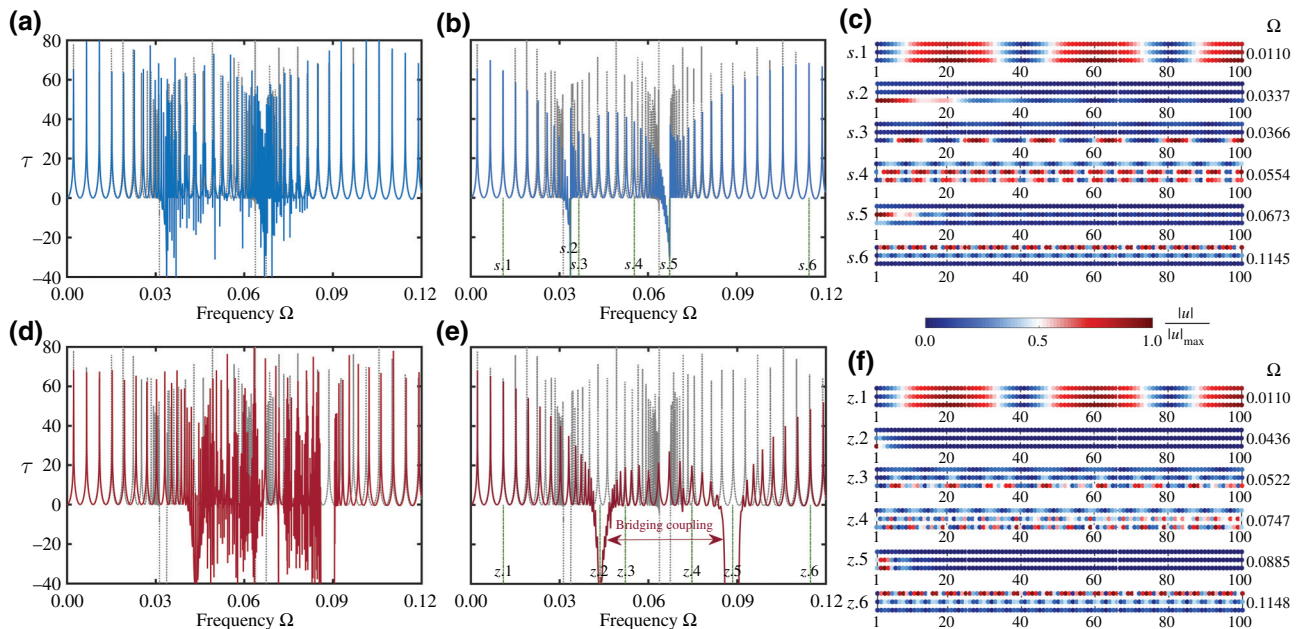

FIG. 3. Transmission response for the isomers with straight [blue lines in (a),(b)] and zigzag [red lines in (d),(e)] interconnections, and (a),(d) without and (b),(e) with damping. The gray dashed lines correspond to the independent resonator isomer. Normalized magnitude of the displacement field for (c) the isomer with straight "s" interconnection and (f) the isomer with zigzag "z" interconnection at the pass band ($\alpha.1$ and $\alpha.6$), within the LR band gap ($\alpha.2$ and $\alpha.5$) and between the LR band gap ($\alpha.3$ and $\alpha.4$) zones, where α is "s" or "z." The unitary displacement excitation is imposed at the host lattice mass of the unit cell $p = 1$.

Hence, the isomer with zigzag interconnections presents a high density of microlocal vibration resonances with higher intensity and energy exchange than the isomer with straight interconnections.

By including inherent damping in the interconnections (which is present in any elastic medium), modeled here in a simple way by a complex spring, i.e., $k^{c*} = k^c(1 + i\eta)$ with $\eta = 0.01$, the energy transferred from the host lattice is dissipated in the resonant network. Therefore, vibration reduction related to the dispersive negative branches at the high density resonance zones is observed in the transmission responses displayed in Figs. 3(b) and 3(e). Although the transmission spectrum of the isomer with straight interconnection [Fig. 3(b)] is still quite similar to the original isomer with independent resonators, the vibration amplitude is slightly reduced between the LR band gaps due to the weak wave interaction coupling. On the other hand, a special pass band with low amplitude resonances between the hybridization band gaps is observed in the isomer with zigzag interconnection. This pass band is different from the pass band of Fig. 3(b) with large amplitude resonances, and is defined in this work as the bridging-coupling frequency range. In addition to the LR band gaps with normalized bandwidths of $\gamma_1 \approx 0.13$ and $\gamma_2 \approx 0.08$ (where $\gamma = 2[\Omega_u - \Omega_1]/[\Omega_u + \Omega_1]$, Ω_u and Ω_1 are the frequencies of the upper and lower boundaries [50]), the bridging-coupling frequency range provides a low vibration amplitude zone at low frequencies from $0.04 < \Omega < 0.09$ with $\gamma \approx 0.76$. This finding is clear evidence of the emergence of bridging-coupling phenomenon in linear systems, which appears due to waves propagating on the resonant network with negative effective mass features and opposite group velocity that strongly interact with the host lattice wave.

In Figs. 3(c)–3(f) we show the displacement fields of the modified isomers at specific frequencies plotted as a heat map superimposed over the finite lattice with 100 unit cells. At the pass bands, the host lattice masses present high motion amplitude and the vibration patterns are similar in both architectures ($s.1$, $s.6$ and $z.1$, $z.6$). Moreover, before the first LR band gap, host and resonant lattices behave as a unique structure, and after the second LR band gap, only the host masses move while the resonant masses are almost stopped. For the straight interconnection, Fig. 3(c), the resonant masses m^a and m^b act independently inside each LR band gap ($s.2$, $s.5$); the first LR band gap is dominated by the resonant masses m^b while the second LR band gap is dominated by the resonant masses m^a. On the other hand, for the zigzag interconnection, Fig. 3(d), both resonant masses have a high motion amplitude acting to stop the wave at the first unit cells that produces the vibration attenuation at the host lattice ($z.2$, $z.5$). Between the LR band gaps, for the straight interconnection isomer ($s.3$, $s.4$), the resonant mass motion is organized in periodic patterns resembling structural vibration modes since the

propagating waves present only positive group velocity. Although the resonant network masses present high amplitude in relation to the host masses, high amplitude of motion is observed in the host lattice, Fig. 3(b). In the bridging-coupling frequency zone of the zigzag interconnection isomer ($z.3$, $z.4$), i.e., between the LR band gaps, the host lattice masses have a low vibration amplitude, Fig. 3(e), while vibration propagates through the whole resonant metachain. In addition, the resonant mass motion does not present a defined pattern due to overlapping of dispersive branches with opposite group velocity.

Finally, each component of the resonant network with zigzag interconnection plays a role in the bridging-coupling tuning. Its location can be controlled by the dipolar resonator of the independent isomer. In this case, the analytical equation for the frequency splitting can be obtained from the respective terms in Eqs. (1) and by assuming harmonic motion:

$$\omega_{1,2} = \sqrt{\tfrac{1}{2}(\omega_{aba}^2 + \omega_b^2) \pm \tfrac{1}{2}\sqrt{(\omega_{aba}^2 + \omega_b^2)^2 - 4\omega_a^2\omega_b^2}} \quad (4)$$

with $\omega_{aba}^2 = (k_a + k_b)/m_a$; moreover, the first term corresponds to the central frequency and the second term to the splitting frequency. The natural frequencies of the dipolar resonator defined in Eq. (4) can be used to predict the location of the two LR band gaps before the interconnections (i.e., for $k^c = 0$). Therefore, the LR band gaps, and hence the bridging-coupling phenomenon, can be tuned at the desired frequency by changing the values of k^a, m^a and k^b, m^b. The remote interaction between the LR band gaps is independent of the frequency gap distance; however, the vibration attenuation at the bridging coupling is stronger for certain values of k^c. As presented in Fig. 4, where the transmission response varies as a function of k^c, three distinct zones between the LR band gaps create a saddle shape. Therefore, there is an optimal value of k^c that minimizes the vibration amplitude in the region between the local resonant band gaps. Small and large bridging-coupling bandwidths present high vibration amplitude (zone limited by the dashed yellow line in Fig. 4), which creates a design zone for k^c between them (zone limited by the dashed green line in Fig. 4). In addition, while the first local resonant band gap has a small shift to high frequencies, the second local resonant band gap has a large shift to high frequencies; thus, the overall bridging-coupling bandwidth increases when the interconnection springs become stiffer. In conclusion, the best choice for k^c is the largest value inside the design zone since it presents a large bandwidth with low vibration amplitude.

D. Effective properties

As stated in Fang *et al.* [41], the bridging coupling possesses a negative effective mass feature connecting the
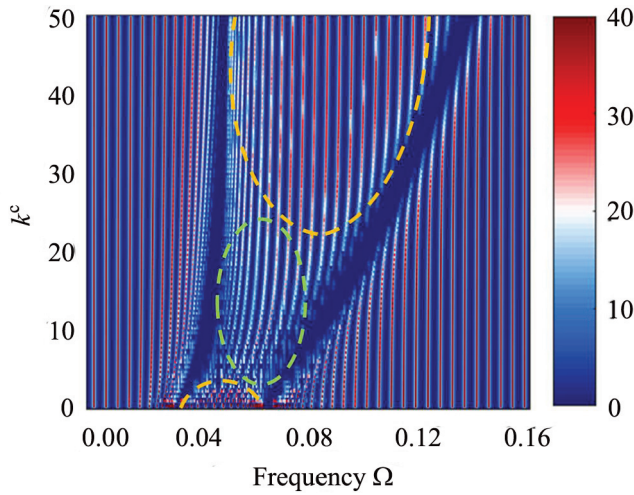
FIG. 4. Parametric analysis of the transmission response as a function of the interconnection stiffness, where the optimal design zone is highlighted between the LR band gaps with a dashed green line.

LR band gaps. In order to confirm the bridging-coupling observation of the previous section, a numerical simulation based on the harmonic approach is used to estimate the effective mass properties at low frequencies under the assumption of large wavelengths compared to metamaterial period, i.e., at frequencies far below the Bragg reflection condition. The approach consists of applying specific harmonic displacements (i.e., perturbations) at the boundaries of the structure and estimating the corresponding induced forces by evaluating the stress average over the boundaries of the structure assumed to be a homogeneous media [51,52]. This technique is also used to compute the effective properties in anisotropic media. The same methodology is applied herein to obtain the effective mass matrix of the metamaterial isomers with multilayer configuration and interlayer interaction. Using frequency response analysis, the effective mass matrix can be determined through the relation

$$\begin{bmatrix} \hat{f}_B^h \\ \hat{f}_B^a \\ \hat{f}_B^b \end{bmatrix} = -\omega^2 \begin{bmatrix} \hat{m}_{\text{eff}}^{hh} & \hat{m}_{\text{eff}}^{ha} & \hat{m}_{\text{eff}}^{hb} \\ \hat{m}_{\text{eff}}^{ah} & \hat{m}_{\text{eff}}^{aa} & \hat{m}_{\text{eff}}^{ab} \\ \hat{m}_{\text{eff}}^{bh} & \hat{m}_{\text{eff}}^{ba} & \hat{m}_{\text{eff}}^{bb} \end{bmatrix} \begin{bmatrix} \hat{u}_B^h \\ \hat{u}_B^a \\ \hat{u}_B^b \end{bmatrix}, \quad (5)$$

where $\hat{u}_B^{i=h,a,b}$ and $\hat{f}_B^{i=h,a,b}$ are the applied displacements and the induced forces on the unit-cell boundaries, respectively. There are two ways to solve the previous system: by imposing forces or displacements. Following Fang et al. [41], the applied force configuration is employed in this work to investigate the bridging-coupling branches with negative effective mass features. In addition, the effective mass of the unit cell considering all the layers can be computed by applying, at the same time, displacement at all boundaries. The displacement phase difference is ignored

due to the assumption of large wavelengths. Hence, the effective mass of the unit cell (or super cell) is numerically computed through the average reaction force on the boundaries as $\tilde{m}_{\text{eff}}(\omega) = \langle \tilde{f}_B \rangle / (-\omega^2 \langle \tilde{u}_B \rangle)$ [53]. Moreover, due to the nonlocal effect in the interconnected configurations, especially in the zigzag interconnections, the numerical effective mass properties are computed using more than one unit cell. By applying a dynamic condensation process on the internal degrees of freedom (DOF) [54], the whole structure can be viewed as a super cell [55,56], and, hence, a similar procedure may be applied to compute these nonlocal effective mass properties. The results are presented in Fig. 5 for all the isomers.

For the isomers with independent and straight interconnection, only one or two unit cells are needed due to the local or quasilocal effective mass properties. Therefore, the long-wavelength assumption is well satisfied. If the resonators in the metamaterial model are independent as in the original isomer, only one effective branch with two local resonances possessing negative effective mass appears, as shown in Fig. 5(a). Considering the resonator interconnections, similar to Fang et al. [41], other effective branches also emerge related to the different layers on the boundaries. These emergent branches influence the vibrational energy transfer between the resonant masses, interaction m^b-m^a, and also from them to the host structure, interaction m^a-m^h. For the straight interconnection, the branch $\hat{m}_{\text{eff}}^{hh}$ [Fig. 5(d) in blue] describes the dipolar band gaps with negative effective mass similar to the previous independent isomer, while the emergent branches $\hat{m}_{\text{eff}}^{hb}$ [Fig. 5(e) in blue] and $\hat{m}_{\text{eff}}^{ha}$ [Fig. 5(f) in blue] respectively have negative and positive effective mass features between the LR band gaps. Considering an applied force in all boundary DOF, these combined branches, leads to an overall effective mass branch $\tilde{m}_{\text{eff}}$ in Fig. 5(b) with negative effective mass around only the upper limit of each LR band gap, and, hence, without nucleating the bridging-coupling phenomenon. Hence, in Fig. 3(c), only a small vibration attenuation in the resonance peaks is observed between the LR band gaps for the isomer with direct interconnections.

Considering the isomer with zigzag interconnections, 6 and 100 unit cells are used due to nonlocal effective mass properties. The branch behavior for $\hat{m}_{\text{eff}}^{hh}$ [Fig. 5(d) in red] and $\hat{m}_{\text{eff}}^{hb}$ [Fig. 5(e) in red] are similar to the straight interconnection configuration, with a shift to high frequencies due to the shift of the LR band gaps when the resonators are interconnected in a zigzag configuration. However, the branch $\hat{m}_{\text{eff}}^{ha}$ [Fig. 5(f) in red] completely changes after the first LR band gap, displaying negative effective mass between the LR band gaps. Therefore, the overall mass branch $\tilde{m}_{\text{eff}}$ in Fig. 5(c) has a negative effective feature connecting the LR band gaps, which is responsible for the remote interaction between the LR band gaps with attenuation properties, and, hence, for the nucleation of the bridging-coupling phenomenon. The effective mass
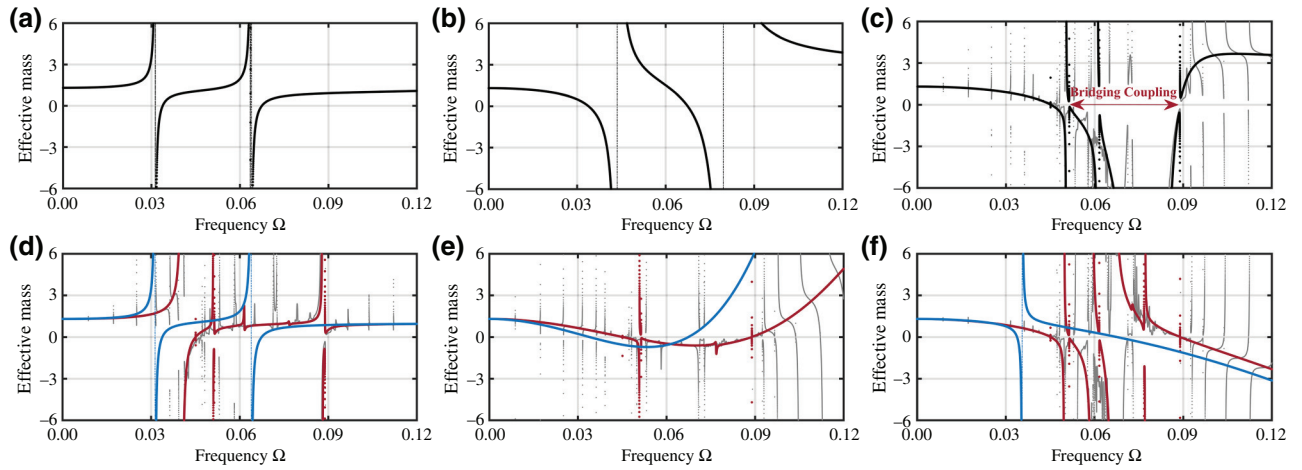
FIG. 5. Effective mass $\tilde{m}_{\text{eff}}$ for the isomer with (a) independent resonators, (b) straight interconnections, and (c) zigzag interconnections. In addition, we also show the branches related to (d) $\hat{m}_{\text{eff}}^{hh}$, (e) $\hat{m}_{\text{eff}}^{hb}$, and (f) $\hat{m}_{\text{eff}}^{ha}$ for the straight configuration (blue), and the zigzag configuration with six unit cells (red) and 100 unit cells (gray).

inversion at the branch $\hat{m}_{\text{eff}}^{ha}$ [Fig. 5(f) in red] comes from the inversion of the group velocity, from positive to negative, related to the branch with an out-of-phase wave mode shape. Therefore, branches with positive-negative group velocity coexist at the same frequency range, with abnormal behavior, nucleating the bridging-coupling frequency range in the linear system. Although the long-wavelength condition cannot be completely satisfied, since some resonances are observed on the branches of the zigzag architecture, the general trend can be clearly observed in Fig. 5(c), confirming our conclusions.

III. PROOF-OF-CONCEPT DEMONSTRATION

In the previous section we presented the concept of bridging-coupling phenomenon using a lattice model. The principle is used in this section to design a three-dimensional (3D) metamaterial rod supporting the desired effect on longitudinal waves. Such continuum realization, which is usually nontrivial, can be useful to visualize applications involving, for example, mechanical, aerospace, and naval systems with superior vibration performance at low frequencies. This design could also be a starting point to propose realizations to observe the same phenomenon in acoustic, electromechanical, or elastic bending media.

To construct the 3D unit cell, we start with the prismatic elastic host rod shown in Fig. 6(a). By attaching two cantilever-in-mass resonators connected in series to both sides of the web, dipolar local resonances are created and the symmetry in relation to the neutral axis is maintained, as shown in Fig. 6(b). Here, the coupled bending-rotational motion (i.e., bending of the resonators as well as rotation of the resonant masses around the z axis) is responsible for attenuating the longitudinal waves, i.e., waves with propagation and polarization in the x axis.

Then, the resonator masses are connected in a zigzag configuration by beams, where m_p^a is connected to m_{p-1}^b and m_{p+1}^b, and m_p^b is connected to m_{p-1}^a and m_{p+1}^a, as shown in Fig. 6(c). The assembly of local resonators and interconnection beams corresponds to the proposed metachain. The interconnection beams also work in bending motion when the masses have a relative motion due to in-phase
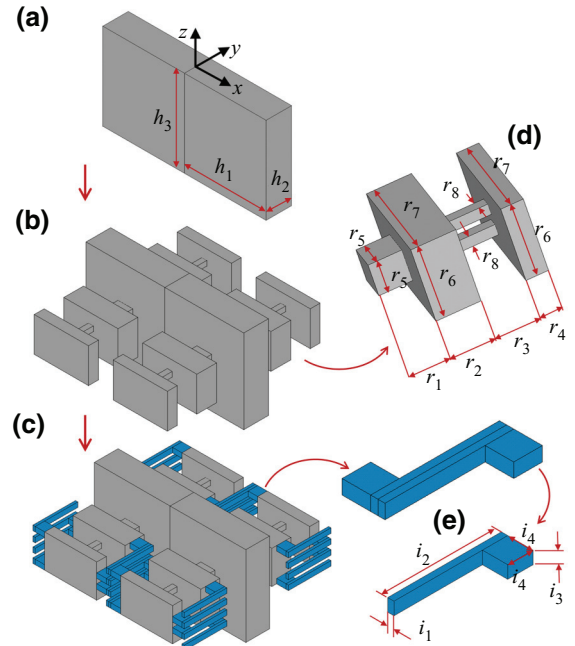

FIG. 6. Design construction of the continuum unit cell: (a) host structure $\rightarrow$ including the local resonators—(b) initial isomer $\rightarrow$ adding the zigzag interconnections—(c) modified isomer. Moreover, we also show (d) the dipolar resonator details and (e) the zigzag interconnection details.

or out-of-phase modes of the dipolar resonator. They are set in four links to keep the internal force balance and to allow only the bending-rotational motion of the masses around the z axis; otherwise, they could rotate around the y axis (torsional motion), and, hence, the bridging-coupling phenomenon could not be clearly observed. In addition, because the 3D metamaterial realization behaves as a continuum model instead of a lumped model, several waves and local resonant band gaps appear in the spectrum of frequencies, and their interaction to nucleate the bridging-coupling phenomenon is also more complex, as presented in the following results.

The proposed metamaterial is constructed using additive manufacturing by layer deposition of polyamide, which behaves as a linear elastic and isotropic material. By performing an experimental harmonic analysis of a rectangular beam (see Appendix A), an initial guess of the material properties is obtained: elastic modulus $E_{IG} = 3.5$ GPa, mass density $\rho_{IG} = 2000$ kg/m^3, and Poisson coefficient $\nu_{IG} = 0.3$. Moreover, the minimum construction geometric dimension of the used 3D printed machine is 1 mm; therefore, the metamaterial design is bounded by this restriction. To design and investigate the validity of the concept, the elastodynamic equations are solved using the finite element (FE) method. Structural SOLID185 elements from Ansys with six nodes and three degrees of freedom per node (i.e., displacements at the three axes u_x, u_y, and u_z) are used to model the unit cell. The FE matrices are extracted from Ansys and the computational codes are written in MATLAB®. Even with more complex behavior, the design methodology follows the analytic concept. First, the local resonances are created by designing the resonators; after that, a parametric analysis is performed on the transmission response by changing the interconnection properties to achieve the desired bridging coupling observation; the final dimensions of the unit cell shown in Fig. 6 are $h_1 = 16$ mm, $h_2 = 3$ mm, $h_3 = 17$ mm, $r_1 = 5$ mm, $r_2 = 4$ mm, $r_3 = 4$ mm, $r_4 = 2$ mm, $r_5 = 3$ mm, $r_6 = 7$ mm, $r_7 = 11$ mm, $r_8 = 1$ mm, $i_1 = 0.5$ mm, $i_2 = 9$ mm, $i_3 = 1$ mm, $i_4 = 2$ mm, with a mass ratio $m_{res}/m_{total} \approx 0.4$.

In Fig. 7 we display the demonstrators for the isomer with resonators in a zigzag interconnection [panel (a)] and for the isomer with independent resonators [panel (b)], both fabricated in a 3D printing machine with 20 unit cells (i.e., total length of 320 mm). Harmonic frequency response analyzes are performed using an electrodynamic shaker to obtain the transmission response $\tau = 20 \log_{10}|u_{out}/u_{in}|$. Moreover, for the continuum model, the normalized frequency is given by $\Omega = \omega h_1/(2\pi c_L)$, where $c_L = \sqrt{E_{IG}/\rho_{IG}}$. Free-free boundary conditions are satisfied by suspending the elastic metamaterial using nylon strings in a rigid frame. For the transmission response, the metastruture is excited through a mini shaker (The Modal Shop's SmartShaker^{TM}, model K2007E01) at one end of the metastructure by using a random noise signal, and the vibration measurements are obtained by accelerometers
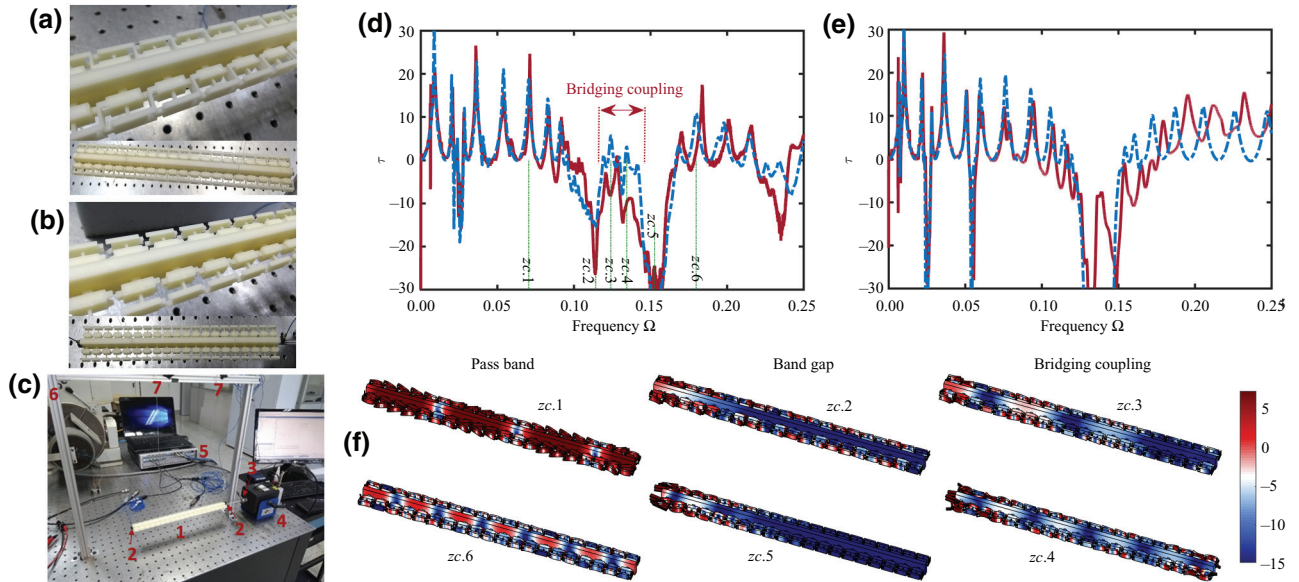

FIG. 7. The metastructure demonstrators constructed in a 3D printed machine with (a) zigzag interconnected resonators and (b) independent resonators. (c) Experimental setup for the harmonic analysis. Here 1 refers to the metastructure, 2 to the accelerometer, 3 to the force transducer, 4 to the shaker, 5 to the data acquisition and signal processing unit, 6 to the frame, and 7 to the string. Transmission response τ obtained by FE simulation (blue) and experiments (red) for (d) the demonstrator shown in (a) and (e) for the demonstrator shown in (b). (f) Selected operational mode shapes for the isomer with zigzag interconnections at the pass band ($zc.1$ and $zc.6$), within the band gap ($zc.2$ and $zc.5$), and at the bridging coupling ($zc.3$ and $zc.4$) zones. The displacement excitation is imposed on the left end of the metastructure in the x direction. These results are similar to those of the lattice model presented in Fig. 3.

TABLE I. Adjusted material properties used in the FE simulations with $\nu = 0.3$ and $\eta = 0.015$.

Component	E (GPa)	ρ (kg/m^3)
Host structure	3.75	1500
Springlike resonator	3.75	1650
Masslike resonator	3.50	1650
Interconnections	3.35	1500

(PCB Piezotronics model 352A24) placed at both ends of the metastructure. Siemens Scadas system is used for the data acquisition and processing. The experimental setup for the spectral testing is shown in Fig. 7(c). These experimental tests are also performed numerically by means of the FE method, where a harmonic input displacement in the x direction is applied at one end and the output displacement is measured at the other end of the metastructure in the same direction. In addition, because the fabrication process induces material variability [25], the material properties for the FE simulation are adjusted around the nominal values to match the experimental results. A trial and error procedure is applied, where the host beam properties are tuned to adjust the first resonance peaks, the local resonators properties are tuned using the LR band gaps, and, afterwards, the interconnection properties are tuned using the behavior of the bridging-coupling frequency range. The adjusted material properties for each component used in the FE simulation are shown in Table I and the procedure described in Appendix B. The same values of material properties are obtained for the components of each demonstrator after the procedure.

Experimental and numerical results agree very well for both demonstrators, as shown in Figs. 7(d) and 7(e). The numerical model represents all the dynamic behavior involved in the experiments, such as the vibration modes at low frequencies and the vibration attenuation zones due to the LR band gaps. Moreover, in Fig. 7(d), the bridging-coupling phenomenon can be clearly observed as a zone with low vibration amplitude ($0.12 < \Omega < 0.14$), presenting 3–4 resonance peaks, between the two LR attenuation zones. The normalized bandwidth (defined in Sec. II C) of each LR band gap is $\gamma_1 \approx 0.20$ and $\gamma_2 \approx 0.16$, respectively, while the bridging-coupling frequency range connects both. Therefore, vibration attenuation is observed within the band gaps, while low amplitude resonances achieved in the special pass band are due to the bridging coupling, resulting in a broad zone of low vibration amplitude with $\gamma \approx 0.55$, which can be enhanced depending on the interconnection properties. For the isomer of Fig. 7(e) with independent resonators, several small band gaps are created at low frequencies and another one at high frequencies with $\gamma \approx 0.23$, which is smaller than the region affected by the band gaps and bridging-coupling frequency range of the modified isomer

with zigzag interconnected resonators. Moreover, the peak inside the band gap around $\Omega = 0.14$ in Fig. 7(e), which is not captured by the numerical model, appears due to spatially variability of material properties [25]. The realization of Fig. 7(d) experimentally demonstrates the proposed bridging-coupling phenomenon in linear metamaterials with a resonant metachain, and shows its superior vibration performance in relation to the traditional metamaterial with independent resonators [Fig. 7(e)]. Although the coupled bending-rotational motion of the resonator masses increases the bandwidth of the first band gap $\Omega \approx 0.11$ (first pillar) and slightly decreases the bandwidth of the second band gap $\Omega \approx 0.15$ (second pillar) that compose the bridging coupling of the zigzag interconnected case (when compared to the independent resonators case at $\Omega \approx 0.05$ and $\Omega \approx 0.14$, respectively), not all coupled bending-rotational motion results in the bridging coupling observed in Fig. 7(d), but the analyzes in this paper show that coupled resonators in a zigzag configuration are needed to achieve this behavior.

The displacement fields numerically computed for the isomer of Fig. 7(a) are shown in Fig. 7(f) as a heat map superimposed over the 3D metastructure. For frequency ranges below the first LR band gap (e.g., $zc.1$), the entire metastructure vibrates (host structure and the metachain), while only the host structure vibrates after the second band gap (e.g., $zc.6$). Inside the LR band gaps, the resonator chain removes energy from the host structure and the vibration is attenuated after a certain number of unit cells (e.g., $zc.2$ and $zc.5$). Finally, at the bridging-coupling zone, the host structure presents low vibration amplitude, while the elastic energy is confined and dissipated in the metachains (e.g., $zc.3$ and $zc.4$) due to structural damping, as presented in Sec. II. These results for the vibration mode shapes are similar to the analytical model and support the design of a continuum model to describe the main physics of the proposed principle. As designed, the resonators only move in phase or out of phase around the z axis without rotation around the y axis. Differently from the lattice model, the components representing the discrete masses in the continuum structure can behave as a rigid (at low frequencies) or deformable body (at high frequencies).

For a more complete analysis, the numerical band structures are obtained after the consideration of the infinite medium model and imposing the Bloch-Floquet periodic boundary conditions on the FE equations of motion of the unit cell [3,31,57]. The material properties presented in Table I of Appendix B are used in the simulations. In addition, all the waves propagate in the x direction, but they present different polarizations in the x direction (longitudinal wave), y direction (transverse bending wave), or z direction (lateral bending wave) respectively shown in Figs. 8(a)–8(c). The waves polarized in the x direction and z direction are coupled because the longitudinal waves are attenuated by the bending-rotational motion of the
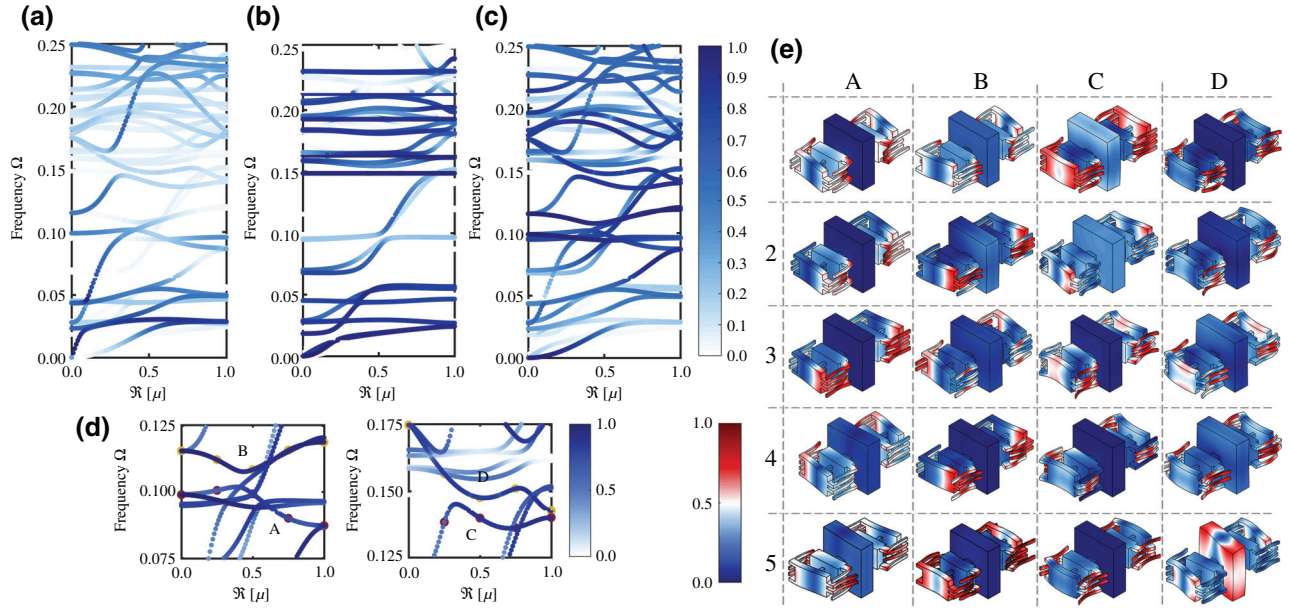
FIG. 8. Band structure of the 3D unit cell using the FE method with wave polarization in the (a) x direction, (b) y direction, and (c) z direction. The graded blue color represents the polarization intensity in the respective axis [57]. The waves polarized in x-z plane are decoupled from the wave polarized in the y axis. The enlarged views in (d) show the branches A-D responsible for nucleating the bridging-coupling phenomenon in (c). (e) Wave mode shapes of branches A (first column), B (second column), C (third column), and D (fourth column) for $\kappa = 0$ (line 1), $\kappa = 0.25$ (line 2), $\kappa = 0.50$ (line 3), $\kappa = 0.75$ (line 4), and $\kappa = 1$ (line 5); the colors represent the normalized magnitude of the displacement field.

resonators (around the z axis), while the waves polarized in the y direction are decoupled from the other directions leastwise at low frequencies. In the x polarization, Fig. 8(a), some LR band gaps appear in the longitudinal waves: two with small bandwidth below $\Omega = 0.05$, one due to veering phenomenon around $\Omega = 0.10$, and another due to locking phenomenon around $\Omega = 0.15$. The gaps at $\Omega = 0.10$ and $\Omega = 0.15$ are the bridge pillars responsible for supporting the bridging-coupling phenomenon that appear due to the dispersive branches with negative effective mass features and overlapping of opposite group velocity.

In the continuum case, two pairs of wave modes with abnormal behavior appear around the band gaps working as the pier in the bridging coupling, which correspond to the proposed concept, as shown in Fig. 8(c). It can also be noted that all the phenomena appear before the first Bragg reflection of the longitudinal wave, which proves the low-frequency behavior. The wave mode shapes at the branches responsible for the bridging coupling are also plotted in a heat map superimposed over the 3D unit cell, which are depicted in Fig. 8(e). In the first pair of wave modes (A-B), the resonator masses behave as quasirigid bodies; however, in the second pair of wave modes (C-D), the masses behave as deformable bodies. The wave modes with abnormal group velocities, with in-phase or out-of-phase mode inversion, and responsible for the bridging coupling, are

also observed in both pairs of wave modes. Finally, in all wave mode shapes, the interconnection beams have high amplitude of motion or deformation; therefore, they play an important role in linking the resonant masses, and in extracting and dissipating the mechanical energy of the host structure within the bridging-coupling frequency zone.

IV. CONCLUSIONS

The bridging-coupling phenomenon was observed in nonlinear acoustic metamaterials with dipolar resonances. A chaotic band reduces the vibration between the linearized LR band gaps when sufficiently large excitation amplitude is imposed to the nonlinear system [19, 41]. Through detailed theoretical analysis and experimental results, we demonstrate that bridging-coupling phenomenon can also emerge in linear systems with a resonant metachain based on a modified isomer of the traditional metamaterial with dipolar resonance. Although this isomer with zigzag interconnections between the resonant masses preserves the static stiffness and mass density, its dispersive behavior possesses noteworthy properties. The resonant branches present negative effective mass features and abnormal group velocity (i.e., overlapping in frequency of positive-negative group velocity) that promotes a remote and strong interaction

between the LR band gaps, and, hence, wave propagation attenuation as well as vibration amplitude reduction between the hybridized band gaps. Therefore, a broadband with low vibration amplitude at low frequencies is obtained regardless of the excitation amplitude.

The literature shows that the performance of linear resonant metamaterials depends on the ratio of the added mass (of the attached resonators) to the original mass of the host structure. By using the proposed principle, the wave and vibration performance of linear metamaterials can be enhanced for a fixed mass ratio. Therefore, the potential applications include a wide range of problems, such as mechanical, aerospace, and naval systems. In addition, the principle only uses the translational motion of resonant masses, and, hence, it can be extended to elastic bending waves as well as to acoustic and electromechanical systems or other medium where it is not possible to explore the translational-rotational coupling [18,27,31–33]. The principle is experimentally observed in an elastic metamaterial rod, whose design can also be extended to systems with periodicity in two (e.g., plates) or three (e.g., solids) dimensions. The fundamentals and the main findings of this demonstration pave avenues for investigating the bridging-coupling phenomenon in linear resonant systems as well as drawing attention to dynamical properties of metamaterial isomers.

APPENDIX A: MATERIAL PROPERTIES ESTIMATION

The initial guess for the material properties is obtained by performing a harmonic analysis for a thin beam with dimensions $l_b = 100$ mm, $h_b = 2$ mm, and $b_b = 10$ mm. A long stroke shaker (Electro-Seis® model APS 113) is used to excite the beam, and the vibration measured at the free end by a portable digital vibrometer (PDV) laser and at the clamped end by an accelerometer. By using a precision mass balance, we estimated the mass density as $\rho_{IG} = 2000$ kg/m^3. Thus, the experimental transmission result, as shown in Fig. 9(b), is compared to a numerical model based on Timoshenko beam theory, which made possible the first estimation (i.e., initial guess) of the elastic properties by matching the natural frequencies: elastic modulus $E_{IG} = 3.5$ GPa and Poisson coefficient $\nu_{IG} = 0.3$. These estimated values minimize the error of the numerical curve in relation to the experimental curve. At low frequencies, below 25 Hz, issues related to the experimental results appear due to the shaker limitation.

APPENDIX B: TRIAL AND ERROR PROCEDURE

Although the manufacturing process in 3D printing is precise for geometric construction, it induces material variability [25]. Moreover, the material properties can change according to the component geometry. Therefore, for an appropriate numerical and experimental comparison, the material properties for each component must be updated. In this work, a trial and error procedure is employed, where the host structure properties are estimated using the low-frequency resonances, the resonator properties are estimated using the LR band gaps characteristics, and, afterwards, the interconnection properties are adjusted using the bridging-coupling behavior. The adjusted properties for all the components are displayed in Table I, where all the components have Poisson ratio $\nu = 0.3$ and structural damping
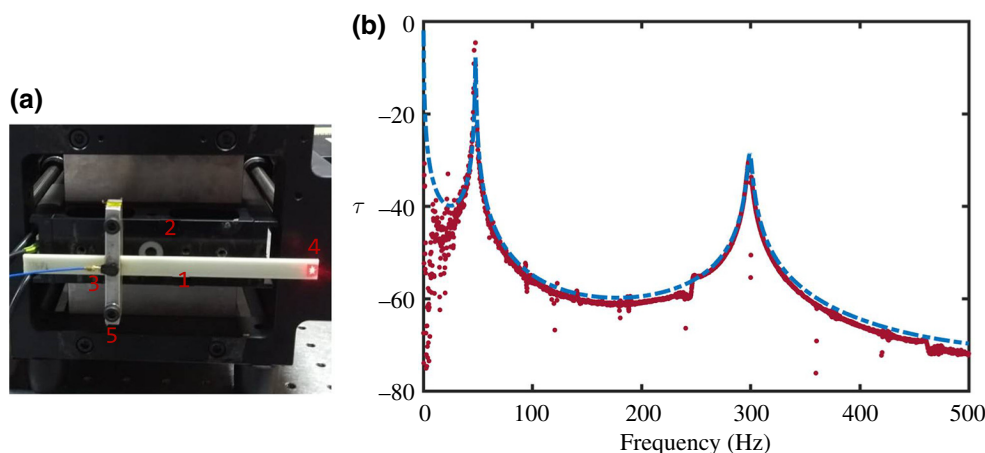

(a)

(b)

FIG. 9. (a) Experimental test setup for properties estimation. Here 1 refers to the thin beam, 2 to the shaker, 3 to the accelerometer, 4 to the laser of the vibrometer Politec PDV, and 5 to the support for the clamped condition. (b) Transmission response used to estimate the initial guess of the material properties obtained through numerical simulation (blue line) and experiments (red circles).

$\eta = 0.015$. The same material properties are used to compute the numerical results for both demonstrators given in Figs. 7(a) and 7(b).

————————

[1] M.-H. Lu, L. Feng, and Y.-F. Chen, Phononic crystals and acoustic metamaterials, Mater. Today **12,** 34 (2009).

[2] M. Maldovan, Sound and heat revolutions in phononics, Nature **503,** 209 (2013).

[3] M. I. Hussein, M. J. Leamy, and M. Ruzzene, Dynamics of phononic materials and structures: Historical origins, recent progress, and future outlook, Appl. Mech. Rev. **66,** 040802 (2014).

[4] J. Christensen, M. Kadic, O. Kraft, and M. Wegener, Vibrant times for mechanical metamaterials, MRS Commun. **5,** 453 (2015).

[5] G. Ma and P. Sheng, Acoustic metamaterials: From local resonances to broad horizons, Sci. Adv. **2,** e1501595 (2016).

[6] S. A. Cummer, J. Christensen, and A. Al, Controlling sound with acoustic metamaterials, Nat. Rev. Mater. **1,** 13 (2016).

[7] B. Assouar, B. Liang, Y. Wu, Y. Li, J.-C. Cheng, and Y. Jing, Acoustic metasurfaces, Nat. Rev. Mater. **3,** 460 (2018).

[8] M. M. Sigalas and E. N. Economou, Elastic and acoustic wave band structure, J. Sound Vib. **158,** 377 (1992).

[9] M. S. Kushwaha, P. Halevi, L. Dobrzynski, and B. Djafari-Rouhani, Acoustic Band Structure of Periodic Elastic Composites, Phys. Rev. Lett. **71,** 2022 (1993).

[10] Z. Liu, X. Zhang, Y. Mao, Y. Y. Zhu, Z. Yang, C. T. Chan, and P. Sheng, Locally resonant sonic materials, Science **289,** 1734 (2000).

[11] J. Zhu, J. Christensen, J. Jung, L. Martin-Moreno, X. Yin, L. Fok, X. Zhang, and F. J. Garcia-Vidal, A holey-structured metamaterial for acoustic deep-subwavelength imaging, Nat. Phys. **7,** 52 (2010).

[12] J. B. Pendry, Negative Refraction Makes a Perfect Lens, Phys. Rev. Lett. **85,** 3966 (2000).

[13] J. Li and C. T. Chan, Double-negative acoustic metamaterial, Phys. Rev. E **70,** 055602 (2004).

[14] N. Fang, D. Xi, J. Xu, M. Ambati, W. Srituravanich, C. Sun, and X. Zhang, Ultrasonic metamaterials with negative modulus, Nat. Mater. **5,** 452 (2006).

[15] S. Yao, X. Zhou, and G. Hu, Experimental study on negative effective mass in a 1D mass—spring system, New J. Phys. **10,** 043020 (2008).

[16] D. Torrent, Y. Pennec, and B. D.-Rouhani, Resonant and nonlocal properties of phononic metasolids, Phys. Rev. B **92,** 174110 (2015).

[17] Z. Jia and L. Wang, Instability-Triggered Triply Negative Mechanical Metamaterial, Phys. Rev. Appl. **12,** 024040 (2019).

[18] C. Yilmaz, G. M. Hulbert, and N. Kikuchi, Phononic band gaps induced by inertial amplification in periodic media, Phys. Rev. B **76,** 054309 (2007).

[19] X. Fang, J. Wen, B. Bonello, J. Yin, and D. Yu, Ultra-low and ultra-broad-band nonlinear acoustic metamaterials, Nat. Commun. **8,** 1288 (2017).

[20] O. R. Bilal, D. Ballagi, and C. Daraio, Architected Lattices for Simultaneous Broadband Attenuation of Airborne Sound and Mechanical Vibrations in All Directions, Phys. Rev. Appl. **10,** 054060 (2018).

[21] R. Al Jahdali and Y. Wu, Coupled resonators for sound trapping and absorption, Sci. Rep. **8,** 13855 (2018).

[22] Y. Zhou, X. Fang, D. Li, T. Hao, and Y. Li, Acoustic Multi-band Double Negativity from Coupled Single-Negative Resonators, Phys. Rev. Appl. **10,** 044006 (2018).

[23] G. Hu, L. Tang, R. Das, S. Gao, and H. Liu, Acoustic metamaterials with coupled local resonators for broadband vibration suppression, AIP Adv. **7,** 025211 (2017).

[24] D. DePauw, H. Al Ba'ba'a, and M. Nouh, Metadamping and energy dissipation enhancement via hybrid phononic resonators, Extreme Mech. Lett. **18,** 36 (2018).

[25] D. Beli, A. T. Fabro, M. Ruzzene, and J. R. F. Arruda, Wave attenuation and trapping in 3d printed cantilever-in-mass metamaterials with spatially correlated variability, Sci. Rep. **9,** 5617 (2019).

[26] P. Celli, B. Yousefzadeh, C. Daraio, and S. Gonella, Bandgap widening by disorder in rainbow metamaterials, Appl. Phys. Lett. **114,** 091903 (2019).

[27] X. N. Liu, G. K. Hu, G. L. Huang, and C. T. Sun, An elastic metamaterial with simultaneously negative mass density and bulk modulus, Appl. Phys. Lett. **98,** 251907 (2011).

[28] A. E. Bergamini, M. Zündel, E. A. Flores Parra, T. Delpero, M. Ruzzene, and P. Ermanni, Hybrid dispersive media with controllable wave propagation: A new take on smart materials, J. Appl. Phys. **118,** 154310 (2015).

[29] E. A. Flores Parra, A. Bergamini, B. Van Damme, and P. Ermanni, Controllable wave propagation of hybrid dispersive media with LC high-pass and band-pass networks, Appl. Phys. Lett. **110,** 184103 (2017).

[30] N. Kherraz, F.-H. Chikh-Bled, R. Sainidou, B. Morvan, and P. Rembert, Tunable phononic structures using lamb waves in a piezoceramic plate, Phys. Rev. B **99,** 094302 (2019).

[31] D. Beli, J. R. F. Arruda, and M. Ruzzene, Wave propagation in elastic metamaterial beams and plates with inter-connected resonators, Int. J. Solids Struct. **139–140,** 105 (2018).

[32] A. O. Krushynska, A. Amendola, F. Bosia, C. Daraio, N. M. Pugno, and F. Fraternali, Accordion-like metamaterials with tunable ultra-wide low-frequency band gaps, New J. Phys. **20,** 073051 (2018).

[33] A. Bergamini, M. Miniaci, T. Delpero, D. Tallarico, B. Van Damme, G. Hannema, I. Leibacher, and A. Zemp, Tacticity in chiral phononic crystals, Nat. Commun. **10,** 8 (2019).

[34] V. F. Nesterenko, C. Daraio, E. B. Herbold, and S. Jin, Anomalous Wave Reflection at the Interface of two Strongly Nonlinear Granular Media, Phys. Rev. Lett. **95,** 158702 (2005).

[35] K. Manktelow, M. J. Leamy, and M. Ruzzene, Multiple scales analysis of wave–wave interactions in a cubically nonlinear monoatomic chain, Nonlinear Dyn. **63,** 193 (2011).

[36] V. J. Sánchez-Morcillo, I. Pérez-Arjona, V. Romero-García, V. Tournat, and V. E. Gusev, Second-harmonic generation for dispersive elastic waves in a discrete granular chain, Phys. Rev. E **88,** 043203 (2013).

[37] N. Nadkarni, C. Daraio, and D. M. Kochmann, Dynamics of periodic mechanical structures containing bistable elastic elements: From elastic to solitary wave propagation, Phys. Rev. E **90**, 023204 (2014).

[38] X. Fang, J. Wen, B. Bonello, J. Yin, and D. Yu, Wave propagation in one-dimensional nonlinear acoustic meta-materials, New J. Phys. **19**, 053007 (2007).

[39] P. B. Silva, M. J. Leamy, M. G. D. Geers, and V. G. Kouznetsova, Emergent subharmonic band gaps in nonlinear locally resonant metamaterials induced by autoparametric resonance, Phys. Rev. E **99**, 063003 (2019).

[40] A. Mojahed, J. Bunyan, S. Tawfick, and A. F. Vakakis, Tunable Acoustic Nonreciprocity in Strongly Nonlinear Waveguides with Asymmetry, Phys. Rev. Appl. **12**, 034033 (2019).

[41] X. Fang, J. Wen, D. Yu, and J. Yin, Bridging-Coupling Band Gaps in Nonlinear Acoustic Metamaterials, Phys. Rev. Appl. **10**, 054049 (2018).

[42] K. H. Matlack, M. Serra-Garcia, A. Palermo, S. D. Huber, and C. Daraio, Designing perturbative metamaterials from discrete models, Nat. Mater. **17**, 323 (2016).

[43] G. W. Milton and J. R. Willis, On modifications of Newton's second law and linear continuum elastodynamics. *Proc. R. Soc. A: Math.*, Phys. Eng. Sci. 463, 855 (2007).

[44] G. Castaldi, V. Galdi, A. Alù, and N. Engheta, Nonlocal Transformation Optics, Phys. Rev. Lett. **108**, 063902 (2012).

[45] A. V. Chebykin, A. A. Orlov, C. R. Simovski, Yu. S. Kivshar, and P. A. Belov, Nonlocal effective parameters of multilayered metal-dielectric metamaterials, Phys. Rev. B **86**, 115420 (2012).

[46] Z. Liu, C. T. Chan, and P. Sheng, Analytic model of phononic crystals with local resonances, Phys. Rev. B **71**, 014103 (2005).

[47] M. L. Cowan, J. H. Page, and P. Sheng, Ultrasonic wave transport in a system of disordered resonant scatterers: Propagating resonant modes and hybridization gaps, Phys. Rev. B **84**, 094305 (2011).

[48] B. R. Mace and E. Manconi, Wave motion and dispersion phenomena: Veering, locking and strong coupling effects, J. Acoustical Soc. Am. **131**, 1015 (2012).

[49] H. W. Park and J. H. Oh, Study of abnormal group velocities in flexural metamaterials, Sci. Rep. **9**, 13973 (2019).

[50] J. H. Oh, S. Qi, Y. Y. Kim, and M. B. Assouar, Elastic Metamaterial Insulator for Broadband Low-Frequency Flexural Vibration Shielding, Phys. Rev. Appl. **8**, 054034 (2017).

[51] R. Zhu, X. N. Liu, G. L. Huang, H. H. Huang, and C. T. Sun, Microstructural design and experimental validation of elastic metamaterial plates with anisotropic mass density, Phys. Rev. B **86**, 144307 (2012).

[52] M. Oudich, B. Djafari-Rouhani, Y. Pennec, M. B. Assouar, and B. Bonello, Negative effective mass density of acoustic metamaterial plate decorated with low frequency resonant pillars, J. Appl. Phys. **116**, 184504 (2014).

[53] X. N. Liu, G. K. Hu, C. T. Sun, and G. L. Huang, Wave propagation characterization and design of two-dimensional elastic chiral metacomposite, J. Sound Vib. **330**, 2536 (2011).

[54] J.-M. Mencik, New advances in the forced response computation of periodic structures using the wave finite element (WFE) method, Comput. Mech. **54**, 789 (2014).

[55] M. M. Sigalas, Elastic wave band gaps and defect states in two-dimensional composites, J. Acoustical Soc. Am. **101**, 1256 (1997).

[56] J. O. Vasseur, P. A. Deymier, B. Djafari-Rouhani, Y. Pennec, and A.-C. Hladky-Hennion, Absolute forbidden bands and waveguiding in two-dimensional phononic crystal plates, Phys. Rev. B **77**, 085415 (2008).

[57] Y.-F. Wang, Y.-S. Wang, and V. Laude, Wave propagation in two-dimensional viscoelastic metamaterials, Phys. Rev. B **92**, 104110 (2015).